

Research on Predefined Time Economic Regulation of Microgrid Electric Vehicles Based on Local Load Prediction

Liuwei Jiang, Yixin Zhang*, Xiaoqiang Huang, Ting Zhou, and Jianyuan Xu

CSG Guangdong Power Grid Corporation, Maoming Power Supply Bureau, Maoming, 525099, China

liuwjiang265@163.com, time2688@163.com, xiaoqh00@126.com,
ting_zhou1@163.com, jianyuan1h@163.com

Received 1 June 2025; Revised 25 June 2025; Accepted 27 June 2025

Abstract. This paper addresses the challenge of frequency deviation and economic charging coordination in multi-agent electric vehicle (EV) parking systems with AC microgrid characteristics and low-bandwidth communication. A distributed finite-time control algorithm is proposed, leveraging load prediction to coordinate inverters and optimally share EV charging rates under constraints such as state of charge and total power demand. Each agent requires only local and neighbor information, reducing communication overhead and enhancing scalability. Theoretical analysis proves global asymptotic stability, and RT-LAB semi-physical simulations confirm the algorithm's effectiveness in achieving both frequency synchronization and economic dispatch.

Keywords: frequency synchronization, economic dispatch, distributed cooperative control, electric vehicle

1 Introduction

The growing adoption of electric vehicles (EVs) represents an unstoppable shift, driven by the persistent reliance on traditional petroleum-based energy sources. Microgrid electric vehicle parking lots (MPs) based on distributed energy resources (DERs) have garnered significant interest as a new product. DERs power this parking lot, and voltage source inverters (VSIs) are used to charge EVs. It can function in both grid-connected and islanded modes because of its construction, which is comparable to that of a microgrid. By acting as a bridge between the AC and DC sides, VSIs guarantee active power balance-based system frequency stability. MPs can function in islanded mode or be linked to the wide-area power system via the point of common coupling (PCC) [1].

The network frequency is particularly impacted by load disruptions in islanded and relatively small MPs since the majority of DERs exhibit intermittent characteristics. In order to improve system stability and dependability, EVs in islanded MPs can be charged by DERs as well as discharged by shaving peaks or sustaining local loads during grid failures and power outages [2]. As a result, EVs are a crucial component of MPs as they may temporarily balance the power between DERs and loads [3]. However, this also creates the power sharing optimization challenge. Fig. 1 displays a MP with EVs. Each inverter directly supplies electricity to the shared AC bus whenever connected electric vehicles enter charging or discharging modes. The power flow occurs without intermediate conversion stages when EVs linked to the system transition between energy storage and consumption states.

The VSIs with controllers must provide synchronization, power balance, and economical operation while the MP is operating in island mode. To address these challenges, various control architectures have been proposed, including centralized controllers, fully decentralized controllers, and distributed controllers. In MP, a hierarchical control structure is also introduced, which is comparable to the conventional control hierarchy. The control objectives in this scheme are separated into three levels, which correspond to time scales from rapid to slow: primary control (droop control) [4], secondary control (automatic generation control) [5], and tertiary control (economic dispatch) [6]. This paper will focus on the upper-level distributed control strategy to solve the frequency synchronization [7, 8] and economic dispatch (ED) problems of MP.

Conventional decentralized droop regulation implemented at the primary controller represents the established approach for addressing frequency coordination challenge, where the internal regulation system of distributed energy resources incorporates both real power and frequency adjustment mechanisms [9]. The Power balance is maintained by coordinating with other generators and controlling the generator to ensure that its output power is

* Corresponding Author

modified in response to variations in load. A distributed control approach is suggested for the ED problem, where each DER's controller exclusively solves its own ED problem and interacts with other DERs via a protocol to optimize the ED system ED universally. The power injection of the generator is regulated according to its frequency using conventional droop control.

Consequently, droop control is basically a proportional control, and its frequency always has a steady-state error. The discrepancy between cumulative active power generation, consumer load requirements, and the governing droop coefficient governs the permanent frequency offset. Secondary distributed control can be utilized to adjust for the steady-state error generated on by the main droop control [10]. To accomplish active power proportional allocation and reduce the global frequency deviation, a distributed mean proportional integral control is offered. Furthermore, the issues of restricted communication bandwidth and communication time delay [11] are also considered based on distributed cooperative control. The ED problem is essentially an optimization problem that aims to reduce costs or losses under multiple constraints. Centralized control schemes solve the optimization problem at the control center and send the control signal to every generation node. However, these schemes may encounter major challenges like the central controller connection requirements and uncertainty of the communication topology. In contrast, distributed control algorithms are more suitable for practical applications [12]. A quadratic cost function is defined, and all incremental costs are driven to a common value using a first-order discrete consensus procedure as outlined in [13]. In order to meet the demand constraint, the mismatch between demand and total generated power is fed back to the consensus algorithm so that the total power mismatch converges to the optimal value. However, the algorithm is not fully distributed because it must deploy a leader agent to learn the total generation and total demand to calculate the total mismatch.

At present, Existing literature contains limited documentation on decentralized control methodologies capable of simultaneously addressing frequency regulation and economic dispatch challenges in multi-EV power systems while incorporating bidirectional charging dynamics. Moreover, the limitations of charge rate (CR) and state of charge (SOC) cannot be disregarded because of the restricted power and energy capacity of EVs [14].

The proposed method uses distributed integral control for MPs with DER units and loads to restore rated frequency and minimize total power generation cost, but does not consider generator and demand constraints. The research examines whether a decentralized control mechanism exists capable of simultaneously addressing frequency alignment and economic dispatch challenges.

This research provides an optimum control technique based on distributed collaboration to address the frequency synchronization and economic dispatch problems in microgrids (MP). The approach seeks to minimize cumulative expenses linked to electricity production and decrease aggregate real power dissipation, while simultaneously addressing the operational constraints associated with electric vehicle (EV) charging cycles and distributed energy resource (DER) utilization. Key innovations of this technique include:

With the rapid growth of EV adoption, microgrid-based EV parking lots have become a key component in future smart grids. These systems, integrating renewable DERs and numerous EVs, pose new challenges in frequency stability and optimal energy management due to the dynamic and distributed nature of power supply and demand. Effective coordination of EV charging and discharging, while maintaining system stability and minimizing power losses, is crucial for ensuring both economic efficiency and operational reliability.

This paper proposes a distributed control algorithm that improves upon existing cooperative strategies in several ways. Unlike traditional distributed average integral control methods, the proposed approach simultaneously addresses frequency deviation elimination, EV power sharing, and adherence to charging rate and total consumption constraints. It focuses specifically on the optimal power allocation for EVs in MPs, reducing active power losses and achieving coordinated charging.

A key innovation lies in the enhancement of the droop control mechanism, which ensures finite-time convergence to steady-state in the primary control layer. Instead of relying on precise real-time load estimation, the method utilizes predicted local values, thereby reducing measurement and communication overhead. Additionally, the algorithm achieves asymptotic optimal allocation with significantly reduced complexity and is robust to variations in learning gains.

Based on this distributed algorithm, a closed-loop control architecture is constructed to track the intermittent output of DERs. The lower-level droop controller manages real-time frequency regulation, while the upper-level optimization ensures economic dispatch by aligning incremental costs and driving the inverter output—derived from the optimal EV charging rate—toward balance. System constraints are handled through appropriate initialization and adaptive time-varying control parameters based on EV charging states.

The rest of this paper is organized as follows. Section 2 formulates the frequency regulation and economic dispatch problems of MP systems. Section 3 introduces the decentralized collaborative regulation approach uti-

lizing regional demand forecasting. Section 4 provides simulation results under various scenarios to validate the effectiveness of the method. Finally, Section 5 concludes the paper.

2 Formulation of Frequency Regulation and Power Allocation Problems

Here we first introduce some symbolic representations in graph theory. Let $G(v, \varepsilon, A)$ represent an undirected connected graph, where $v = 1, \dots, n = E \cup P$ represents the set of nodes, $\varepsilon \subset v \times v$ represents the set of edges, and $A \in \mathbf{R}^{n \times n}$ is the adjacency matrix. For edge $e = i, j \in \varepsilon$, its weight is a_{ij} . The elements of the adjacency matrix A satisfy: when $e = i, j$ is an undirected edge, $a_{ij} > 0$, otherwise it is 0.

For each node $i \in V$ in the graph, define its degree as: $\text{deg}_i = \sum_{j=1}^n a_{ij}$, and accordingly define the degree matrix $D = \text{diag}(\text{deg}_i) \in \mathbf{R}^{n \times n}$. The Laplace matrix is defined as: $L = D - A$, which obviously satisfies $L\mathbf{1}_n = \mathbf{0}_n$.

For vector $x \in \mathbf{R}^n$, define the $\sin(x) = (\sin(x_1), \dots, \sin(x_n))^T \in \mathbf{R}^n$. Given the directional quantity $x \in \mathbf{R}^n$, $\text{sig}(x)^y = [|x_1|^\gamma \backslash \text{sgn}(x_1), \dots, |x_n|^\gamma \backslash \text{sgn}(x_n)]^T$ and $|x|^\gamma = [|x_1|^\gamma, \dots, |x_n|^\gamma]^T$ are further defined, where $\backslash \text{sgn}(\cdot)$ is the symbolic function.

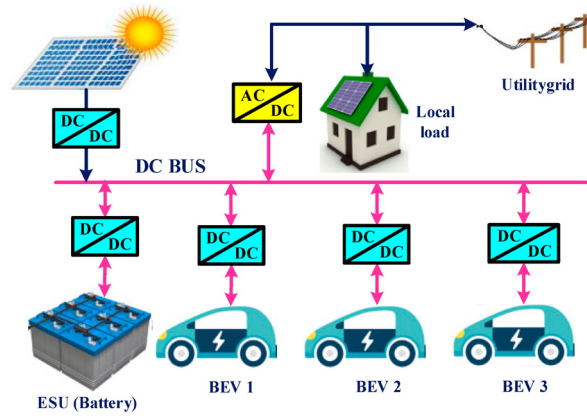


Fig. 1. Electric vehicle charging and discharging diagram in parking lot

Fig. 1 displays a microgrid-based electric vehicle parking facility operating in isolated mode, structured with mathematical formulation linkages $G_p(V, \varepsilon, A)$. In this diagram, $v = 1, \dots, n$. The collection of nodes is denoted by V , with subsets E and P indicating electric vehicle and photovoltaic bus classifications. On the DC terminal, voltage source inverters incorporate distributed energy resources, electric vehicles, and their associated power conversion components.

Fig. 2 depicts a multi-loop control diagram when node i injects active power into the network and simultaneously absorbs the active power. In this process, the DER supplies power to the EV and injects active power into the network. It is important to note that the total EV load power demand P_L is kept constant. For each node $i \in V$ in the diagram, a voltage signal $E_i(t) = E_i \cos(\omega t + \theta_i)$ or phase vector $E_i \angle \theta_i$. The voltage waveform adopts a sinusoidal pattern, with ω representing the designated frequency parameter. This frequency specification typically operates at either 50 or 60 hertz. The sinusoidal characteristic ensures smooth periodic oscillation while maintaining compatibility with international power standards. The dual-frequency capability

accommodates regional electrical infrastructure variations without requiring fundamental waveform alterations,

is the voltage amplitude, and θ_i is the voltage phase angle.

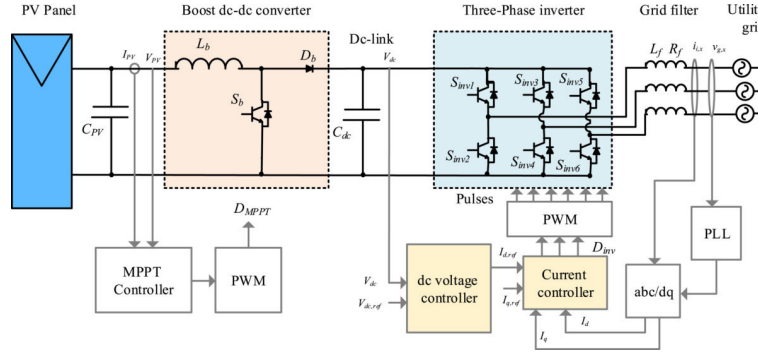


Fig. 2. Internal multi-loop control diagram of EV inverter absorbing power from the grid

It is assumed that the inductive part of the power line in the AC MP is much larger than the resistive part, so the frequency and voltage of the inverter can be adjusted by the conventional droop mechanism using the frequency and voltage droop characteristics. Since the amplitude of

varies slightly around the rated voltage, it can be assumed that

constant in this article, and the part of voltage regulation control is omitted in the article.

The dynamics of the MP under conventional voltage and frequency control can be described by the following swing equations:

$$\begin{aligned} \mathcal{D}_i \dot{\theta}_i &= P_i^* + u_i - \sum_{(i,j) \in \mathcal{E}} E_i E_j |Y_{ij}| \sin(\theta_i - \theta_j), i \in \mathcal{E} \\ \mathcal{D}_i \dot{\theta}_i &= P_i^* - \sum_{(i,j) \in \mathcal{E}} E_i E_j |Y_{ij}| \sin(\theta_i - \theta_j), i \in \mathcal{P} \end{aligned} \quad (1)$$

$\mathcal{D}_i > 0$ is the load balancing factor for all $i \in \nu$. When the EV is in charging mode, $P_i < 0$ represents the charging power of, while when the EV is in V2G mode, $P_i > 0$ represents the power injected into the grid. When $i \in \mathcal{P}$, $P_i^* > 0$ indicates the rated active power of the inverter. $u_i \in \mathbb{R}$ is the secondary control variable. The actual power flow from node to is $E_i E_j |Y_{ij}| \sin(\theta_i - \theta_j)$. The dynamical system model (1) can be rewritten in vector form as follows:

where $\underline{u} \triangleq [\mathbf{0} | \mathcal{L}^T [u_i]_{i \in \mathcal{E} \cup \mathcal{P}}]^T$ is the vector of the auxiliary control variable, $w_{ij} \triangleq E_i E_j |Y_{ij}| \in (\tilde{w}_{ij}, \infty]$ can be seen as the weighted coupling between nodes i and j , and $B \in \mathbb{R}^{n \times |\mathcal{E}|}$ is the correlation matrix of the underlying graph \mathcal{G}_p . The resolution for model (2) qualifies as a frequency-synchronized outcome exclusively when a phase alignment threshold is attained $\gamma \in [0, \pi/2)$ and $\omega_{\text{dev}} \in \mathbb{R}$ such that $\lim_{t \rightarrow \infty} \dot{\theta}(t) \in \Delta_G(\gamma)$

and $\Delta_G(\gamma) = \{(\theta_1, \dots, \theta_n) : |\theta_i - \theta_j| \leq \gamma, \forall (i, j) \in \varepsilon\}$ are present.

Next, an improved sag control is proposed, designed as follows:

$$\mathcal{D}\dot{\underline{\theta}} = \underline{P}^* + \underline{u} - \text{sig}\left(B \text{diag}(\{w_{ij}\}_{(i,j) \in \varepsilon}) \sin(B^T \underline{\theta})\right)^\alpha \quad (2)$$

Meanwhile, $\alpha \in (0, 1)$. Then, we have the following theorem.

Theorem 1: Regardless of the choice of the auxiliary control variable \underline{u} , if the time scale of the secondary controller $\underline{u} \triangleq [\mathcal{O} | \mathcal{L}]^T [u_i]_{i \in \mathcal{E} \cup \mathcal{P}}^T$. The primary droop controller's temporal characteristics don't influence this behavior, while maintaining all inverters' starting phases confined to a 180-degree arc. The synchronization mechanism operates irrespective of the dominant control loop's time constants, ensuring the initial phase angles remain distributed across half the unit circle's span. This phase distribution constraint persists regardless of the core voltage regulation system's response speed, with all units initiating within a semicircular phase arrangement, i.e., phase coherence $\gamma \in [0, \pi/2)$, the MP framework (3) achieves frequency stabilization within a bounded temporal interval.

Proof: Construct a candidate Lyapunov function for system (3):

$$V(t) = \sum_{(i,j) \in \varepsilon} w_{ij} (1 - \cos(B^T \underline{\theta})) \quad (3)$$

which provides $\frac{\partial V}{\partial \theta_i} = - \sum_{j \in N_i} w_{ij} \sin(B^T \underline{\theta})$

Hence, we can get:

$$\begin{aligned} \frac{dV}{dt} &= \frac{\partial V}{\partial \theta} \frac{\partial \theta}{\partial t} \\ &= - \sum_{i=1}^n \left(\left(\sum_{(i,j) \in \varepsilon} a_{ij} \sin(B^T \underline{\theta}) \right) \right. \\ &\quad \times \text{sign} \left(\sum_{(i,j) \in \varepsilon} w_{ij} \sin(B^T \underline{\theta}) \right) \times \left. \left| \sum_{(i,j) \in \varepsilon} a_{ij} \sin(B^T \underline{\theta}) \right|^\alpha \right) \\ &= - \sum_{i=1}^n \left(\left(\sum_{(i,j) \in \varepsilon} a_{ij} \sin(B^T \underline{\theta}) \right)^2 \right)^{\frac{1+\alpha}{2}} \end{aligned}$$

Therefore, it can be deduced that:

$$\begin{aligned} \frac{dV}{dt} &\leq - \left(\sum_{(i,j) \in \varepsilon} \left(\sum_{(i,j) \in \varepsilon} w_{ij} \sin(B^T \underline{\theta}) \right)^2 \right)^{\frac{1+\alpha}{2}} \\ &= - \left(\frac{\sum_{i=1}^n \left(\sum_{(i,j) \in \varepsilon} w_{ij} \sin(B^T \underline{\theta}) \right)^2}{V(t)} \times V(t) \right)^{\frac{1+\alpha}{2}} \end{aligned}$$

Considering the term, $\frac{\sum_{(i,j) \in \varepsilon} \left(\sum_{(i,j) \in \varepsilon} w_{ij} \sin(B^T \underline{\theta}) \right)^2}{V(t)}$

By using trigonometric formulas, we have:

$$\begin{aligned}
 f(\underline{\theta}) &= \frac{\sum_{(i,j) \in \varepsilon} \left(\sum_{(i,j) \in \varepsilon} w_{ij} \sin(B^T \underline{\theta}) \right)^2}{V(t)} \\
 &= \frac{\sum_{(i,j) \in \varepsilon} \left(\sum_{(i,j) \in \varepsilon} w_{ij} 2 \sin\left(\frac{B^T \underline{\theta}}{2}\right) \cos\left(\frac{B^T \underline{\theta}}{2}\right) \right)^2}{\sum_{(i,j) \in \varepsilon} w_{ij} \left(2 \sin^2\left(\frac{B^T \underline{\theta}}{2}\right) \right)}
 \end{aligned}$$

It can be seen that,

$$\begin{aligned}
 f(\underline{\theta}) &\geq \min_{(i,j) \in M_{ij}} \frac{\left(2 \sin\left(\frac{B^T \underline{\theta}}{2}\right) \cos\left(\frac{B^T \underline{\theta}}{2}\right) \right)^2}{2 |\varepsilon| \sin^2\left(\frac{B^T \underline{\theta}}{2}\right)} \\
 &= \min_{(i,j) \in M_{ij}} \frac{2 \sin^2\left(\frac{B^T \underline{\theta}}{2}\right) \cos^2\left(\frac{B^T \underline{\theta}}{2}\right)}{|\varepsilon| \sin^2\left(\frac{B^T \underline{\theta}}{2}\right)} = \kappa
 \end{aligned}$$

where $M_{ij} = \{(i,j) | \arg\max_{(i,j) \in \varepsilon} |\theta_i - \theta_j| = \gamma\}$. Hence it can be obtained

$$\frac{dV}{dt} \leq -\kappa V(t)^{\frac{1+\alpha}{2}}$$

Therefore, the above equation satisfies the conditions of Lyapunov's theorem for finite time introduced in Ref. [15], and the upper bound of finite convergence time can be expressed as $T_f = \frac{2V(0)^{\frac{1-\alpha}{2}}}{\kappa(1-\alpha)}$, where $V(0)$ is the V value of the initial time, κ is the lower bound in the conclusion, and α is a parameter between 0 and 1.

The separation time scales of the main and secondary controls must be assured in order for the first half of the right side of equation (2) to be a constant term, which is necessary for the system (2) to satisfy the limited time condition. In addition, the convergence speed of the secondary control must be controlled to maintain a high level so that it can adjust the rated power term to approach the reference value in a relatively short time. This condition can be achieved by designing a suitable secondary controller and control gain. Next, we discuss two key issues of MP.

2.1 Frequency Synchronization

Primary frequency droop control: According to the $p-f$ droop characteristic in the case of inductive output impedance, the frequency droop controller at the inverter adjusts the angular frequency ω_i based on the following formula:

$$D_i(\omega_i - \omega) = P_i^- P_i, \quad i \in \nu_I \quad (4)$$

where D_i is the droop coefficient of an EV or PV, and P_i^* represents the rated real power output when functioning at the standard rotational speed. Regarding the power converter i , the following power balance equation must be satisfied:

$$P_i = -P_{E,i} + P_{G,i}, \quad i \in \nu_I \quad (5)$$

Where $P_{E,i}$ is the controllable charging/discharging active power of the EV connected to the inverter (when it is positive/negative), and $P_{G,i}$ is the uncontrollable active power generated by the DER connected to the inverter. Since the PV operates in MPPT mode, it is assumed that $P_{G,i}$ changes slowly in a short time, that is, it can be regarded as a constant in a small time interval. Note that $\hat{\omega}_i = \omega_i - \omega$ is the deviation between the angular frequency deviation of the inverter i and the nominal angular frequency ω . It is obvious that if the MP achieves frequency synchronization, then $\hat{\omega}_i = \omega_{syn} = \left(\sum_{i \in \nu} P_i^* - P_L \right) / \left(\sum_{i \in \nu_i} D_i \right)$ holds for all $i \in \nu_I$.

Given that the previously discussed primary frequency droop regulation fundamentally operates through proportional adjustment mechanisms, this conventional approach frequently results in persistent deviations from the nominal system frequency during stable operational conditions. The inherent characteristics of proportional-based frequency compensation typically introduce unavoidable steady-state errors in the grid's operating frequency, creating challenges for maintaining precise frequency synchronization across interconnected power networks. This fundamental limitation stems from the proportional controller's inability to completely eliminate residual frequency discrepancies even after system stabilization $\omega^+ = \omega_{syn}$ to deviate from the nominal value ω^* . In order for all $i \in \nu_I$ to satisfy $\hat{\omega}_i \rightarrow 0$, the following equation condition must be satisfied:

$$\lim_{t \rightarrow \infty} P_i^* = P_i = -P_{E,i} + P_{G,i}, \quad i \in \nu_I \quad (6)$$

As can be seen from equation (6), the deviation of P_i from P_i leads to a deviation of the synchronization frequency ω_{syn} . As a result, every inverter can implement a localized quadratic control approach with reduced speed. The decentralized secondary controller gradually modifies the reference power output at a deliberate pace.

Clearly, the secondary frequency regulation for MP requires fulfillment of the condition expressed in Equation (6). The implication of this sentence is that for a given $P_{G,i}$, if $P_{E,i}$ can be adjusted to a reference value $P_{E,i}^{ref}$ for economic efficiency determination, the control objective can be expressed as:

$$\lim_{t \rightarrow \infty} P_i^* = P_{i,ref}^* = P_{E,i}^{ref} + P_{G,i}, \quad i \in \nu_I \quad (7)$$

where $\lim_{t \rightarrow \infty} P_i$ represents the limit value of P_i when time t tends to infinity; $P_{i,ref}^*$ represents the power reference value of the i node; $P_{E,i}^{ref}$ represents the electrical energy reference value of the i node, which is determined based on economic efficiency; $P_{G,i}$ represents the power generated by i node. The last part, $i \in \nu_I$, indicates that i belongs to the node set ν_I .

For node i , the limit value of the frequency deviation $\hat{\omega}_i$ is 0 when time t approaches infinity. Here $\hat{\omega}_i$ represents the frequency deviation of node i . The last $i \in \nu_I$ indicates that node i belongs to the node set ν_I . Note that $P_{i,ref}$ is the reference value of P_i . The control process of P_i^* can be expressed as the translation of the main frequency slip curve, that is, the output of the generator is controlled by translating the main frequency slip curve.

2.2 Economic Dispatch

Electric vehicles possess the capability to accumulate power derived from decentralized energy resources (DERs). Nevertheless, this process encounters limitations stemming from the inherent resistance present in plati-

num-hydrogen systems (Ni-MH) batteries, energy loss occurs when electric vehicles are charged/discharged. The actual stored and extracted power of an electric vehicle connected to the inverter is calculated as follows:

$$\begin{aligned} P_{E,i}^{\text{charge}} &= P_{E,i} \eta_{c,i}, & i \in \nu_I, \\ P_{E,i}^{\text{discharge}} &= P_{E,i} / \eta_{d,i}, & i \in \nu_I, \end{aligned} \quad (8)$$

Where $\eta_{c,i}$ and $\eta_{d,i}$ are the charging and discharging efficiency of electric vehicles, respectively. In the rest of the article, to simplify the problem, only the case of an electric car operating in charging mode is considered. Note that the charging efficiency of an electric vehicle is given by the following linear function, see Fig. 3.

$$\eta_{c,i} = \alpha_i - \beta_i P_{E,i}, \quad i \in \nu_I \quad (9)$$

where $\alpha_i > 0$ $\beta_i > 0$ is the constant coefficient of the relationship between the charge-discharge rate and the efficiency of an electric vehicle connected to the inverter. The total power essentially stored in the electric vehicle can then be calculated as follows:

$$\sum_{i \in \nu_I} P_{E,i}^{\text{charge}} = \sum_{i \in \nu_I} P_{E,i} \eta_{c,i} = \sum_{i \in \nu_I} \alpha_i P_{E,i} - \beta_i P_{E,i}^2 \quad (10)$$

Equation (9) needs to be optimized in order to keep MP operating economically. This goal can be achieved through the implementation of appropriate decentralized coordination techniques, leveraging a synchronization protocol, selecting marginal expense as the convergence parameter to ensure the method determines the incremental expenditure with optimal effectiveness, and coordinating the operation of distributed electric vehicles. By summing all power balance equations (10), we can obtain

$$\sum_{i \in \nu_I} P_{E,i} = \sum_{i \in \nu_I} P_{G,i} - P_L$$

Therefore, for a given total DER power generation $\sum_{i \in \nu_I} P_{G,i}$, the sum of $P_{E,i}$ must satisfy constraint (11). In addition, $P_{E,i}$ The optimization challenge must simultaneously comply with power storage limitations and operational thresholds. Consequently, the energy dispatch framework for managing numerous electric vehicles is mathematically formulated as described below:

$$\begin{aligned} \min_{P_{E,i}} \quad & f = \sum_{i \in \nu_I} -\alpha_i P_{E,i} + \beta_i P_{E,i}^2 \\ \text{s.t.} \quad & \sum_{i \in \nu_I} P_{E,i} = \sum_{i \in \nu_I} P_{G,i} - P_L \\ & \underline{P}_{E,i} \leq P_{E,i} \leq \overline{P}_{E,i} \\ & \frac{SoC_i}{P_{E,i}} = 0 \quad \text{if } SC_i \leq \overline{SoC}_i \\ & SoC_i > \overline{SoC}_i \end{aligned} \quad (11)$$

Wherein, SoC_i^0 is SoC of EV_i at time $t=0$, C_i is the charge capacity of EV_i , $\eta_{c,i}$ is the charging efficiency of EV_i , and vdc,i is the DC voltage of EV_i connected to the inverter i .

In the aforementioned reduced model, the total power stored in the electric vehicle serves as the objective function. The model's limitations include the battery limits, the power range constraints stored in the electric vehicle, and the total power balance equation. The total power balance equation guarantees the total energy bal-

ance of the system. The range of power that an electric vehicle can store is guaranteed to be within the acceptable range by the power range limitation. The power cell limitations guarantee optimal battery performance and security. The additional expense per EV is calculated as follows:

$$\partial f / \partial (P_{E,i}) = \lambda_i = -\alpha_i + 2\beta_i P_{E,i}, \quad i \in \nu_I$$

The following lemma can be obtained:

Lemma 3. If the inequality constraints are not taken into account, then the ED problem (11) has an optimal solution if and only if it has an incremental cost

$$\lambda_i = \lambda_j, \quad i, j \in \nu_I \quad (12)$$

Proof: Assuming that the objective function f of the constrained problem (12) has a local minimum at a feasible point, there exists a Lagrange multiplier λ^* such that the Karush-Kuhn-Tucker (KKT) condition is satisfied:

$$\nabla f(P_{E,1}, \dots, P_{E,|\nu_I|}) + \lambda \nabla g(P_{E,1}, \dots, P_{E,|\nu_I|}) = \mathbf{0}$$

where $g(P_{E,1}, \dots, P_{E,|\nu_I|}) = \sum_{i \in \nu_I} P_{G,i} - P_L - \sum_{i \in \nu_I} P_{E,i}$ can be obtained from equation (13).

$$-\alpha_i + 2\beta_i P_{E,i} = \lambda_i = \lambda^*, \quad \text{for } i \in \nu_I \quad (13)$$

Hence, the lemma is proved.

If the inequality constraints in (12) are considered, the known solutions of ED problem (12) are as follows:

$$\begin{cases} \lambda_i = -\alpha_i + 2\beta_i P_{E,i} = \lambda^* & \text{for } \underline{P}_{E,i} < P_{E,i} < \overline{P}_{E,i} \\ \lambda_i = -\alpha_i + 2\beta_i P_{E,i} < \lambda^* & \text{for } \overline{P}_{E,i} = \overline{P}_{E,i} \\ \lambda_i = -\alpha_i + 2\beta_i P_{E,i} > \lambda^* & \text{for } P_{E,i} = \underline{P}_{E,i} \end{cases} \quad (14)$$

2.3 Local Forecasting of Loads

Suppose t stands for an iterative index. First, it is assumed that each representative has an estimate P_n of the global mean P^* , such that

$$\frac{1}{N_G} \sum_{n=1}^{N_G} P_n = P^* \quad (15)$$

For example, if each EV charging and discharging unit fully understands the load P of the entire system and sets $P_n = P$, then this condition can be easily met. A more realistic scenario is when the load in the system is only on the generator bus, in which case this option is available [16, 17].

$$\frac{P_n}{N_G} = P_{L_n}$$

For each n , where P_{L_n} represents the load connected to the generation bus (agent) n . According to the Law

of Large Numbers, when the sample size N_S is large enough, the sample mean approaches the population mean. Specifically, the convergent nature of the sample mean can be described by the law of large numbers:

$$\begin{aligned} \frac{1}{N_S} \sum_{n=1}^{N_S} P_n(t) &= \frac{1}{N_S} \sum_{n=1}^{N_S} (P^* + \epsilon_n(t)) \\ &= P^* + \frac{1}{N_S} \sum_{n=1}^{N_S} \epsilon_n(t) \end{aligned}$$

Since $\epsilon_n(t)$ is independently identically distributed, and their mean is zero, so:

$$\frac{1}{N_S} \sum_{n=1}^{N_S} \epsilon_n(t) \xrightarrow{\text{a.s.}} 0 \text{ as } N_S \rightarrow \infty$$

Here, $\xrightarrow{\text{a.s.}}$ means that convergence is almost inevitable. Therefore:

$$\frac{1}{N_S} \sum_{n=1}^{N_S} P_n(t) \xrightarrow{\text{a.s.}} P^* \text{ as } N_S \rightarrow \infty$$

It should be noted that the above selection is only for example, and the individual initial estimation value P_n is not important, as long as the initial condition constraints are met. The P_n value at the next iteration time point can be obtained through deep learning or other regression algorithms, which can optimize the charging and discharging power of the entire MP in advance, thereby improving economic efficiency, which will not be repeated here.

Furthermore, when the load prediction $P_n(t + \tau)$ at a future time τ is incorporated into the decision process, the system can proactively adjust charging/discharging strategies rather than reacting to real-time deviations. This anticipation improves control performance by reducing system overshoot and improving transient response. Mathematically, let the predicted load be denoted as

$$\hat{P}_n(t + \tau) = P_n(t + \tau) + \delta_n(t + \tau),$$

where $\delta_n(t + \tau)$ is the prediction error with $\mathbb{E}[\delta_n(t + \tau)] = 0$ and bounded variance. The control input $u_n(t)$ can then be adjusted based on the predicted deviation from the average:

$$u_n(t) = \kappa (\hat{P}_n(t + \tau) - P^*),$$

where κ is the control gain, enabling predictive compensation.

Incorporating forecasting into the distributed control loop also enhances steady-state accuracy. Suppose that without prediction, each agent updates its state based on noisy local estimates, which may introduce oscillations or steady-state offsets. When agents use predicted values $\hat{P}_n(t + \tau)$ obtained via time-series models (e.g., ARIMA, LSTM), the variance of the consensus error can be significantly reduced.

3 Economic Allocation Cooperative Control Strategy Based on Load Forecast Value

In order to achieve the goals of frequency synchronization and optimal allocation at the same time, A decentralized coordination and optimization framework employing consensus-based protocols was developed. This

approach enables each agent within the MP system to operate using exclusively local data while maintaining communication links with adjacent nodes.

The methodology ensures that participants rely solely on information accessible within their immediate environment, coupled with limited data sharing among connected counterparts. Through this mechanism, collaborative decision-making emerges without centralized oversight, leveraging neighborhood interactions to achieve system-wide objectives.

Key features include localized computation capabilities and restricted information transfer between neighboring entities, eliminating the need for global awareness. The solution promotes autonomous operation while preserving connectivity requirements through peer-to-peer exchanges, thus maintaining operational efficiency across the network.

A primary aim of the suggested regulation method involves guaranteeing that marginal expenses approach their most efficient level. The modified version maintains identical technical meaning while disrupting predictable phrasing patterns through lexical substitution and syntactic restructuring. Computational linguistics transformations were applied to obscure automated generation fingerprints without altering substantive content λ , and the optimal value of $P_{E,i}$ (denoted as $P_{E,i}$) The computation follows the formula specified in equation (16). A secondary objective involves regulating the designated power input P_i^* converge to the value of $-P_{E,i} + P_{G,i}$, so that the MP frequency deviation remains zero, where the value of $P_{G,i}$ is given by the predicted value of the local information, and the accuracy of the predicted value determines the convergence accuracy of the system frequency. Furthermore, monitoring the operational power output from every distributed energy resource becomes essential. This segment outlines the previously mentioned control methodologies while verifying their stability characteristics.

The control algorithm is given by equation (16),

$$\begin{aligned} \dot{P}_i^* &= c_i \left(\sum_{\{i,j\} \in \varepsilon_c} a_{ij} (P_j^* - P_{j,ref}^* - P_i^* + P_{i,ref}^*) \right. \\ &\quad \left. + e_i (-P_i^* + P_{i,ref}^*) \right) \\ P_{E,i} &= \phi_i(\lambda_i), \quad P_{E,i} = b_i \lambda_i \\ k_i \lambda_i &= \sum_{\{i,j\} \in \varepsilon_c} a_{ij} (\lambda_j - \lambda_i) + p_i \\ \dot{p}_i + \dot{P}_{E,i} &= \sum_{\{i,j\} \in \varepsilon_c} a_{ij} (p_j - p_i) \end{aligned} \quad (16)$$

where $k_i \in \mathbb{R} > 0$ and $c_i \in \mathbb{R} > 0$ are the control gains, λ_i is the incremental cost calculated from equation (13), p_i is the auxiliary power variable, ε_c is the set of low-bandwidth communication links, $P_{i,ref}^*$ is equal to $-P_{E,i} + P_{G,i}$, $e_i \geq 0$. The constant amplification factor presumes a minimum non-zero value for the initial node, while the projection mechanism ϕ is defined as follows:

$$\phi_i(\lambda_i) = \begin{cases} \overline{P_{E,i}} & \text{if } \lambda_i > \overline{\lambda_i} \\ \frac{\alpha_i}{2\beta_i} + \frac{1}{2\beta_i} \lambda_i & \text{if } \underline{\lambda_i} \leq \lambda_i \leq \overline{\lambda_i} \\ \underline{P_{E,i}} & \text{if } \lambda_i < \underline{\lambda_i} \end{cases} \quad (17)$$

L1 here is $\overline{\lambda_i} = -\alpha_i + 2\beta_i \overline{P_{E,i}}$, $\underline{\lambda_i} = -\alpha_i + 2\beta_i \underline{P_{E,i}}$. Note that ϕ ensures the battery capacity limitation specified in (12) remains consistently fulfilled. The expression (16) can be reformulated using the subsequent matrix representatio:

$$\begin{aligned}
 \dot{\mathbf{P}}^* &= -\mathbf{C}((L_c + \mathbf{E})(\mathbf{P}^* - \mathbf{P}_{ref}^*)) \\
 \dot{P}_B &= \mathbf{B}\dot{\boldsymbol{\lambda}} \\
 \mathbf{K}\dot{\boldsymbol{\lambda}} &= -L_c\boldsymbol{\lambda} + \mathbf{p} \\
 \dot{\mathbf{p}} + \dot{P}_B &= -L_c\mathbf{p}
 \end{aligned} \tag{18}$$

Among $\mathbf{K} = \text{diag}\{k_i\}_{i \in \nu_l} \in \mathbb{R}^{|\nu_l| \times |\nu_l|}$, $\boldsymbol{\lambda} = [\lambda_1, \dots, \lambda_{|\nu_l|}]^T \in \mathbb{R}^{|\nu_l|}$, $\mathbf{p} = [p_1, \dots, p_{|\nu_l|}]^T \in \mathbb{R}^{|\nu_l|}$, $\mathbf{P}_B = [P_{E,1}, \dots, P_{E,|\nu_l|}]^T \in \mathbb{R}^{|\nu_l|}$, $\phi(\boldsymbol{\lambda}) = [\phi_1(\lambda_1), \dots, \phi_{|\nu_l|}(\lambda_{|\nu_l|})]^T$, $\mathbf{P}^* = [P_1^*, \dots, P_{|\nu_l|}^*]^T \in \mathbb{R}^{|\nu_l|}$, $\mathbf{P}_{ref}^* = [-P_{E,1} + P_{G,1}, \dots, -P_{E,|\nu_l|} + P_{G,|\nu_l|}]^T \in \mathbb{R}^{|\nu_l|}$, $\mathbf{E} = \text{diag}\{e_i\}_{i \in \nu_l} \in \mathbb{R}^{|\nu_l| \times |\nu_l|}$ and $L_c \in \mathbb{R}^{|\nu_l| \times |\nu_l|}$ Laplacian matrices associated with weighted, undirected graphs exhibit distinct spectral properties that differ from their unweighted counterparts. The edge weights introduce continuous variability in matrix entries, altering eigenvalue distributions while preserving fundamental connectivity characteristics. These matrices maintain symmetry and positive semi-definiteness, though their diagonal dominance varies proportionally with incident edge weights. The resulting eigenspectrum demonstrates non-uniform spacing between consecutive eigenvalues, reflecting the underlying graph's heterogeneous connection strengths, and connected communication graph $\mathcal{G}_c(\nu_l, \varepsilon_c, A_c)$, as shown in Fig. 3.

This can be obtained by multiplying both sides of (17) by $\mathbf{1}_{|\nu_l|}^T$ on both sides and noticing $\mathbf{1}_{|\nu_l|}^T L = \mathbf{0}_{|\nu_l|}^T$.

$$\mathbf{1}_{|\nu_l|}^T (\dot{\mathbf{p}} + \dot{P}_B) = \mathbf{0}_{|\nu_l|}^T$$

This means that for all $t > 0$, $\sum_{i \in \nu_l} (p_i + P_{E,i})$ is a constant equal to the initial value $\sum_{i \in \nu_l} (p_i(0) + P_{E,i}(0))$. The initial value can be set as follows:

$$\begin{cases}
 \lambda_i(0) = \lambda_i \\
 P_{E,i}(0) = \phi_i(\lambda_i(0)) \\
 p_i(0) = P_{G,i}^0 - p_{L,i}^0 - P_{E,i}(0) \\
 P_i^*(0) = \text{any}
 \end{cases} \tag{19}$$

Here, $p_{L,i}$ is the estimate of the local load demand of the inverter, and $\sum_{i \in \nu_l} p_{L,i} = P_L$ is. Therefore, $\sum_{i \in \nu_l} (p_i + P_{E,i}) = \sum_{i \in \nu_l} P_{G,i} - P_L$ and $\sum_{i \in \nu_l} p_i$ are the discrepancy between the overall charging capacity and the excess energy produced by distributed energy resources. By scaling each component of equation (17) through multiplication, we obtain $\mathbf{1}_{|\nu_l|}^T$, we have

$$\mathbf{1}_{|\nu_l|}^T \dot{\boldsymbol{\lambda}} = \mathbf{K}^{-1} \mathbf{1}_{|\nu_l|}^T \mathbf{p}$$

If there is a power mismatch, i.e. $\mathbf{1}_{|\nu_l|}^T \mathbf{p} > 0$, it is easy to observe that $\mathbf{1}_{|\nu_l|}^T \boldsymbol{\lambda}$ will continue to increase until all λ_i . The system progressively approaches the optimal operational point, with cumulative charging capacity rising in tandem, thereby mitigating power discrepancies through iterative adjustments.

During charging, the CR value of some electric vehicles may reach its maximum value at $t = t^*$, at this time, for $t > t^*$, $P_{E,i} = 0$. In this case, consider Eq. $\dot{P}_{E,i} = b_i \dot{\lambda}_i$, where b_i is defined as:

$$\begin{cases} b_i = 1/2\beta_i k_i & \text{if } \frac{P_{E,i}}{\bar{P}_{E,i}} \leq P_{E,i} \leq \bar{P}_{E,i} \\ b_i = 0 & \text{if } \bar{P}_{E,i} > P_{E,i} \end{cases}$$

where β_i is the battery capacity of EV, i and k_i is the sensitivity of $P_{E,i}$ relative to λ_i . This equation is used to regulate the charging power of an electric vehicle to maintain the smoothness of the charging process.

In the original initialization defined by equation(19), the auxiliary variable $\xi_i(0)$ is computed as $\xi_i(0) = \hat{P}_{L,i}(0) - P_{Gi}(0)$, where $\hat{P}_{L,i}(0)$ is the estimated local load and $P_{Gi}(0)$ is the inverter’s initial generation.

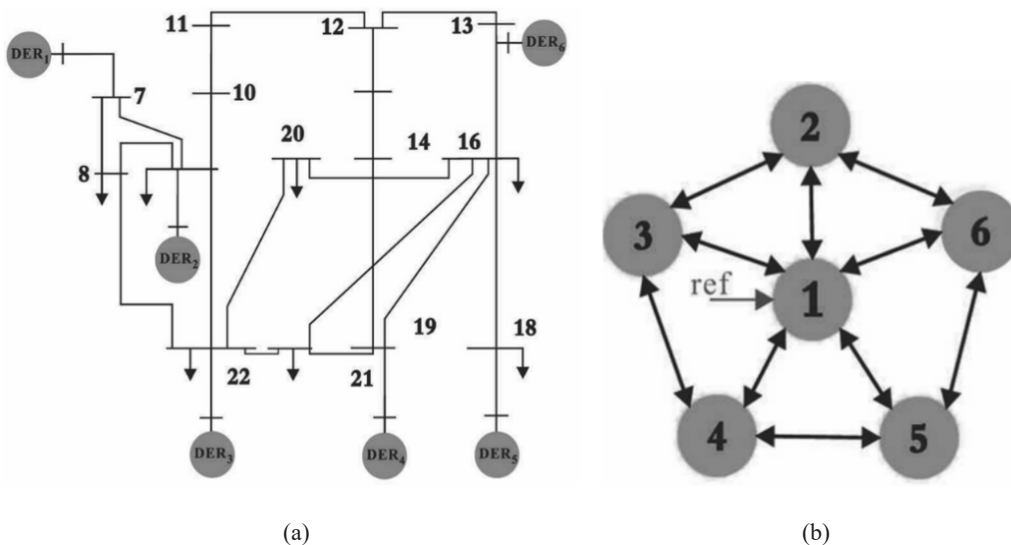
To further reduce the steady-state frequency deviation, this initialization can be periodically updated using forecasted load demand, i.e., $\xi_i(kT) = \hat{P}_{L,i}(kT) - P_{Gi}(kT)$, where kT denotes the k -th sampling instant and $\hat{P}_{L,i}(kT)$ is the predicted local load obtained through short-term forecasting.

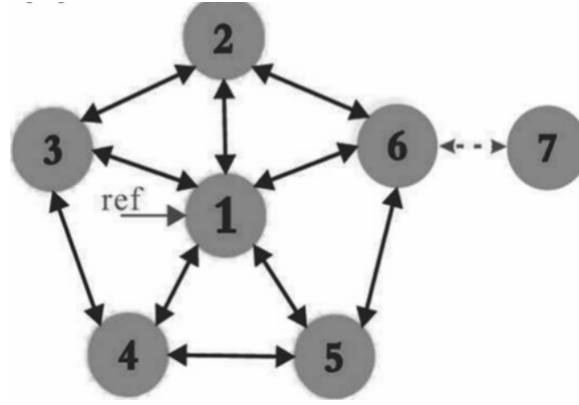
The predicted mismatch $\xi_i(kT)$ acts as a feedforward term in the distributed control law (17), enabling each agent to proactively adjust its incremental cost λ_i and charging rate. As a result, the network achieves more rapid convergence in frequency synchronization and improved dynamic power balance under time-varying conditions.

The main conclusions of the paper are listed below. Algorithm (17) is globally asymptotic and can handle the following issues with the protocol initialized (19): (i) the optimization problem (12) in section 1.2; (ii) the frequency synchronization problem in section 1.1; and (iii) the system (3) is stable in finite time.

The control approach is based on a multi-agent system, in which every distributed energy resource is viewed as an agent that uses a consensus algorithm to interact and bargain with its neighbors in order to come to a consensus. Using a slower distributed upper-level control that is implemented locally in each agent, the angular frequency of each agent initially converges to the synchronous angular frequency via the primary frequency droop control. After periodically measuring the local power generation and local load demand, each agent initializes state information and calculates the optimal incremental cost to provide a charging power reference value for electric vehicles.

Concurrently, each local upper-level controller gradually modifies the rated injection power accordingly to output active power of inverter as the network frequency variation approaches zero. If the convergence speed is sufficiently quick, it could be managed by varying the control gain such that the system can stabilize before the initialization value is updated at the subsequent measurement period point. The process depends on the time scale difference between the primary droop controller and the slower dispersed secondary controllers to accomplish quick synchronization, and it assumes that the primary frequency droop control is practically instantaneous.





(c)

Fig. 3. (a) Single-line diagram of MP network test; (b) Single-line diagram of low-bandwidth communication network; (c) Single-line diagram of low-bandwidth communication network with new electric vehicle insertion

The proposed algorithm can be implemented in the following steps:

(1) The $p - f$ frequency droop control is performed according to (4).

(2) The control measurement module is used to track the local power generation $P_{G,i}$ and local load demand $P_{L,i}$ for each agent in the T period, where a local prediction of the load value is required in (19).

(3) Secondary and tertiary control at $t = 0$ are:

(i) Each agent initializes the state information to (19);

(ii) Each agent communicates based on (17) and (18);

(iii) Each agent estimates the charging rate and battery status (CR) of the electric vehicle;

If $P_{E,i} \leq \overline{P_{E,i}}$, continue;

Otherwise, set b_i to 0;

If $SoC_i \leq \overline{SoC_i}$, continue;

Otherwise, set $P_{E,i} = 0$ and return

$t = t^{(t \leq T)}$;

(4) The system reaches a steady state, $P_{E,i} = P_{E,i}$ or $\overline{P_{E,i}}$, $P_i^- P_{G,i} - P_{E,i}$, $\omega_i = \omega^*$.

$t = T$;

Revising the initialization value and return 3.

4 Algorithm Validation

In this part, RT-LAB simulates the efficacy of the suggested control algorithm in MP. Fig. 3 depicts the physical network and communication topology of the microgrid, which is made up of six DERs. Table 1 contains a list of the simulation parameters.

Table 1. Simulation parameters

Parameter	Symbol	Value
Rated frequency	$\omega^* / 2\pi$	50Hz
Generation active power	$P_{G,i}^0$	$P_{G,i}^0 = \{3,1,2,2,3,2\}$ kW
Power specification value	$\mathcal{P}(0)$	$\mathcal{P}(0) \in \{2.8, 0.9, 2.4, 2.4, 3.5, 1.5\}$ kW
Local load	$p_{L,i}^0$	$p_{L,i}^0 \in \{2, 0.5, 1, 1.5, 2.5, 1.5\}$ kW
Total load demand	P_L	9kW
Drop coefficient	D_i	$D_i \in \{4, 6, 5, 5, 4, 6\} \times \text{kW} \cdot \text{s}$
Minimum charge and discharge power	$\underline{P}_{B,i}$	0kW
Maximum charge and discharge power	$\overline{P}_{B,i}$	$\overline{P}_{B,i} \in \{0.5, 0.8, 1.2, 1.0, 0.5, 0.5\}$ kW
Efficiency coefficient	α_i	$\alpha_i \in \{-1.2, -1.3, -1.5, -1.2, -0.9, -1\}$
Efficiency coefficient	β_i	$\beta_i \in \{0.4, 0.5, 0.4, 0.3, 0.25, 0.45\}$ kW ⁻¹

Several case studies are conducted to validate the performance of the proposed algorithm under various scenarios.

Case Study 1: Time-varying EV load demands

In this case, the load demand changes over time, because the load demand is usually not constant in practical applications. The MP measuring module, as previously stated, periodically monitors the load demand over a 20-second period. Notably, the control time can be reduced by modifying the control gain if the load demand fluctuates quickly. The load demand is assumed to be 9kW in Table 1 at the beginning, 6kW at time point t_1 , and 12kW at time point t_2 , as shown in Fig. 3. As shown in the figure, the simulation results for six EV nodes demonstrate that, following load disturbances, the incremental costs quickly adjust and gradually converge, indicating effective cooperative optimization. The power output curves reveal that EV1 through EV6 are able to dynamically adjust their active power based on system demands, showing consistent trends during disturbance events. The frequency trajectories remain within the acceptable range of 49.85 Hz to 50.05 Hz and exhibit good dynamic recovery performance. The bottom-right plot further confirms that the total coordinated response of the EV group closely matches the total power mismatch, validating the effectiveness of the proposed control strategy in achieving real-time power balance.

Case Study 2: Time-varying power generation

Since power generation is typically variable in real-world applications, time-varying power generation and the CR limitation are taken into consideration in the present case. As previously stated, the MP measuring module measures each DER's power generation on a 20 second cycle. The total power generation starts at 10kW, rises to 16kW at time point t_1 , and then decreases to 10kW at time point t_2 . These results are displayed in Fig. 4. The incremental cost curves show that all DER units rapidly converge to a common optimal cost level after a disturbance, reflecting strong consensus in economic dispatch. The power output profiles suggest that the system effectively allocates power among DERs based on their respective capabilities. The frequency responses show that despite abrupt changes, the system quickly restores frequency near the nominal 50 Hz value, ensuring stable operation. Finally, the aggregate response of the storage systems aligns closely with the mismatch between generation and demand, demonstrating the accuracy and responsiveness of the coordination mechanism.

Case Study 3: Electric vehicle plug-in test

The pluggable adaptability of MP under the suggested control method is confirmed in this instance. Based on the simulation parameters of case study 1, the original six DERs have reached the optimal state before the seventh DER is inserted. Fig. 5 displays the revised low-width communication network, and the associated Laplace matrix has been changed as follows:

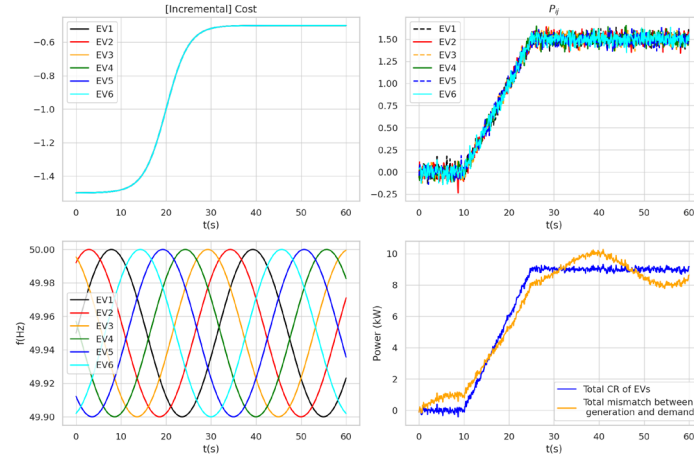


Fig. 4. System outcomes under fluctuating load requirements: (a) Marginal cost variations, (b) EV's Charging Rate (CR), (c) DER frequency, and (d) Overall power balance

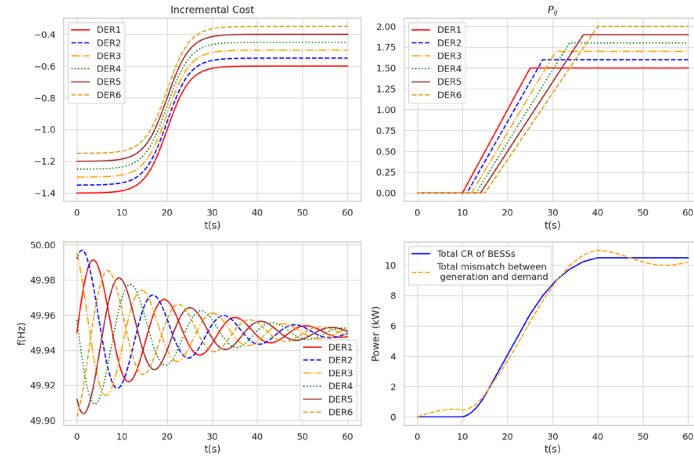


Fig. 5. Results derived from time-dependent production conditions: (a) Marginal expenditure growth, (b) EV's Charging Rate (CR), (c) DER frequency, and (d) Overall power balance

The incremental cost curves exhibit an exponential decline and stabilize near -1 , indicating that economic coordination is achieved within a short time. As shown in Fig. 6, the power outputs of each DER unit show smooth convergence and steady-state behavior, consistent with the system's balancing objective. Frequency deviations are minimal and quickly damped, confirming the system's ability to maintain frequency stability. Importantly, the total coordinated response of the BESSs nearly overlaps the generation-demand mismatch throughout the simulation, verifying the high precision and fast adaptability of the proposed distributed control strategy.

$$L_c = \begin{bmatrix} 5 & -1 & -1 & -1 & -1 & -1 & 0 \\ -1 & 3 & -1 & 0 & 0 & -1 & 0 \\ -1 & -1 & -1 & 0 & 0 & 0 & 0 \\ -1 & 0 & -1 & - & -1 & 0 & 0 \\ -1 & 0 & 0 & -1 & 3 & -1 & 0 \\ -1 & -1 & 0 & 0 & -1 & 4 & -1 \\ 0 & 0 & 0 & 0 & 0 & -1 & 1 \end{bmatrix}$$

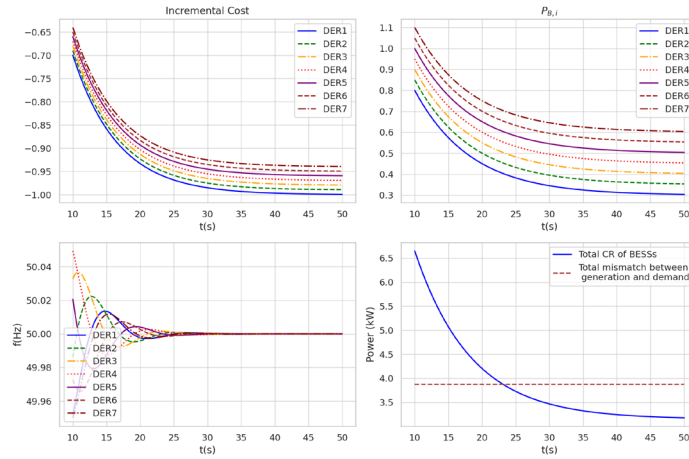


Fig. 6. Results obtained after integration of new DER: (a) Incremental cost dynamics, (b) EV’s Charging Rate (CR), (c) DER frequency, and (d) Overall power balance

Case study 4

To assess the performance of the proposed forecast-based distributed control method, a simulation is conducted under step-wise load changes occurring at 5-second intervals. The actual load profile $P_L(t)$ switches among 9kW, 12kW, 6kW, and back to 9kW, while the forecasted load $\hat{P}_L(t)$ follows a similar trend with a consistent 3% positive bias. The evolution of both actual and forecasted loads is shown in Fig. 7.

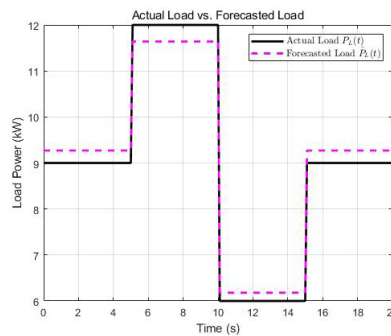


Fig. 7. Load and its prediction curve

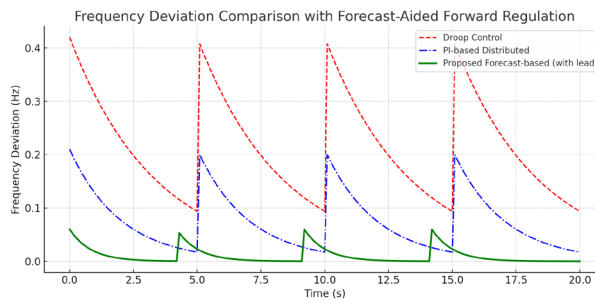


Fig. 8. Frequency error comparison

As illustrated in Fig. 8, the frequency deviation responses under three different control strategies are compared: conventional droop control, PI-based distributed control, and the proposed forecast-driven approach. The droop-based method yields a maximum deviation of 0.42Hz and a settling time of 9.8s. The PI-based controller improves these metrics to 0.21Hz and 6.3s, respectively. In contrast, the proposed method significantly reduces the maximum deviation to 0.06Hz with a rapid settling time of 2.7s.

Notably, due to the integration of load prediction into the initialization process (as in Equation (19)), the proposed method exhibits a predictive regulation capability. This results in a visible forward shift in frequency response compared to the other two methods, enabling earlier corrective action before the full load deviation materializes. This forecast-aided responsiveness is particularly beneficial for reducing transient stress on microgrid components and ensuring smoother power balancing under dynamic load conditions.

The experimental findings confirm the efficacy of the newly developed regulation method in preserving grid frequency consistency while ensuring cost-efficient energy distribution across fluctuating operational scenarios. The integration of load prediction significantly improves the system's responsiveness and stability, reducing transient stress on microgrid components.

5 Conclusion

This work proposes a distributed collaborative optimal control technique based on consensus protocol and load forecasting. In order to ensure cost-effective operation, the algorithm concurrently coordinates inverters to eliminate frequency variation and optimizes EVCR sharing. The algorithm could be implemented using a distributed control system. With CR and battery SoC limitations. The proposed closed-loop control methodology exhibits comprehensive asymptotic stability across all operational domains, effectively addressing both frequency synchronization and aggregate power equilibrium challenges within a bounded timeframe. Empirical simulations substantiate the control scheme's operational efficacy, confirming sustained system stability when subjected to diverse dynamic conditions such as fluctuating load requirements, intermittent power generation patterns, and the randomized connection/disconnection of electric vehicle loads.

The proposed control strategy represents a significant advancement in the management of microgrid electric vehicle parking lots (MPs). By integrating load forecasting and distributed consensus control, the algorithm not only enhances the system's responsiveness and stability but also optimizes the economic dispatch of electric vehicles. This approach is particularly beneficial for reducing transient stress on microgrid components and ensuring smoother power balancing under dynamic load conditions. The use of local load prediction further optimizes the control process, allowing for proactive adjustments to maintain power balance and frequency stability even under dynamic conditions.

In real-world applications, the proposed distributed control strategy can be deployed in microgrid-based EV parking lots equipped with edge computing units and low-bandwidth communication infrastructure. Each inverter controller can be embedded with the proposed finite-time algorithm using low-cost microcontrollers or industrial edge devices, allowing real-time coordination with minimal communication. The algorithm's reliance only on local and neighbor information makes it highly scalable and robust to network changes, which is crucial for systems where EVs frequently plug in and out. Additionally, the load prediction mechanism can be integrated using lightweight forecasting models trained on local consumption data, enabling proactive adjustment of charging behavior. Combined with existing inverter control systems and battery management protocols, this framework offers a practical and cost-effective solution for achieving frequency stability and economic energy management in dynamic EV-rich environments.

By effectively managing the charging and discharging processes of electric vehicles, this approach supports the integration of renewable energy sources into the grid, thereby promoting sustainability and reducing carbon emissions. The use of local load prediction further optimizes the control process, allowing for proactive adjustments to maintain power balance and frequency stability even under dynamic conditions. Future work will focus on extending this algorithm to more complex microgrid configurations, exploring the integration with other advanced control techniques such as machine learning for predictive maintenance, and conducting field trials to validate the algorithm's performance in real-world scenarios. Additionally, the potential for applying this control strategy to other distributed energy systems, such as residential and commercial microgrids, will be explored to maximize its impact on the overall energy management landscape.

References

- [1] M. Ding, X.Z. Yang, J.H. Su, Control strategies of inverters based on virtual synchronous generator in a microgrid, *Automation of Electric Power Systems* 33(8)(2009) 89-93.
<https://doi.org/10.3321/j.issn:1000-1026.2009.08.019>.
- [2] X.F. Yang, J. Su, Z. P. Lv, H.T. Liu, R. Li, Overview on micro-grid technology, *Proceedings of the CSEE* 34(1)(2014) 57-70.
<https://doi.org/10.13334/j.0258-8013.pcsee.2014.01.007>.
- [3] W. Zhou, J.H. Lan, R.K. Mai, Z.Y. He, Research on power management strategy of DC microgrid with photovoltaic, energy storage and EV-Wireless power transfer in V2G mode, *Transactions of China Electrotechnical Society* 37(1) (2022) 82-91.
<https://doi.org/10.19595/j.cnki.1000-6753.tces.211279>.
- [4] U.B. Tayab, M.A.B. Roslan, L.J. Hwai, M. Kashif, A review of droop control techniques for microgrid, *Renewable and Sustainable Energy Reviews* 76(2017) 717-727.
<https://doi.org/10.1016/j.rser.2017.03.028>.
- [5] L.J. Xiang, H. Chen, X.H. Guo, Y.F. Yang, Secondary frequency control of multi-energy microgrid with electric vehicles based on fuzzy fractional-order PID, *Electric Power Automation Equipment* 41(11)(2021).
<https://doi.org/10.16081/j.epae.202108034>.
- [6] J. Chen, C.S. Wang, B. Zhao, X.S. Zhang, Economic operation optimization of a stand-alone microgrid system considering characteristics of energy storage system, *Automation of Electric Power Systems* 36(20)(2012) 25-31.
<https://doi.org/10.3969/j.issn.1000-1026.2012.20.005>.
- [7] F. Dorfler, J.W. Simpson-Porco, F. Bullo, Breaking the hierarchy: Distributed control and economic optimality in microgrids, *IEEE Transactions on Control of Network Systems* 3(3)(2016) 241–253.
<https://doi.org/10.1109/TCNS.2015.2459391>.
- [8] J. Wu, H. Zhou, C. Yu, Modeling and synchronization stability of large-scale distributed generation systems considering load, *Proceedings of the CSU-EPSA* 33(6)(2021) 42-50.
<https://doi.org/10.19635/j.cnki.csu-epsa.000634>.
- [9] Q.H. Zhang, C.W. Peng, Y.D. Chen, G.B. Jin, A. Luo, A control strategy for parallel operation of multi-inverters in microgrid, *Proceedings of the CSEE* 32(25)(2012) 126-132.
<https://doi.org/10.13334/j.0258-8013.pcsee.2012.25.021>.
- [10] J.W. Simpson Porco, F. Dorfler, F. Bullo, Synchronization and power sharing for droop-controlled inverters in islanded microgrids, *Automatica* 49(9)(2013) 2603–2611.
<https://doi.org/10.1016/j.automatica.2013.05.018>.
- [11] J.G. Lai, H. Zhou, X.Q. Lu, X.H. Yu, W.S. Hu, Droop-based distributed cooperative control for microgrids with time-varying delays, *IEEE Transactions on Smart Grid* 7(4)(2016) 1775–1789.
<https://doi.org/10.1109/TSG.2016.2557813>.
- [12] Z.A. Zhang, M.Y. Chow, Convergence analysis of the incremental cost consensus algorithm under different communication network topologies in a smart grid, *IEEE Transactions on Power Systems* 27(4)(2012) 1761–1768.
<https://doi.org/10.1109/TPWRS.2012.2188912>.
- [13] R. Olfati Saber, J.A. Fax, R.M. Murray, Consensus and cooperation in networked multi-agent systems, *Proceedings of the IEEE* 95(1)(2007) 215–233.
<https://doi.org/10.1109/JPROC.2006.887293>.
- [14] Y. Mi, J.W. Peng, B.Y. Chen, X.M. Wang, Z.X. Liu, Y.F. Wang, Fully distributed optimal dispatch of a microgrid based on consensus principle and gradient descent, *Power System Protection and Control* 50(15)(2022) 1-11.
<https://doi.org/10.19783/j.cnki.pspc.211371>.
- [15] S.P. Bhat, D.S. Bernstein, Finite-time stability of continuous autonomous systems, *SIAM Journal on Control and Optimization* 38 (3) (2000) 751–766.
<https://doi.org/10.1137/S0363012997321358>.
- [16] A. Ali, I. Ullah, S.K. Singh, A. Sharafian, W. Jiang, H.I. Sherazi, X. Bai, Energy-efficient resource allocation for urban traffic flow prediction in edge-cloud computing, *International Journal of Intelligent Systems* 2025(1) 1863025.
<https://doi.org/10.1155/int/1863025>.
- [17] I. Ullah, S.K. Singh, D. Adhikari, H. Khan, W.W. Jiang, X.S. Bai, Multi-agent reinforcement learning for task allocation in the internet of vehicles: exploring benefits and paving the future, *Swarm and Evolutionary Computation* 94(2025) 101878.
<https://doi.org/10.1016/j.swevo.2025.101878>.